JOURNAL OF GEOPHYSICAL RESEARCH, VOL. 114, A04207, doi:10.1029/2008JA013816, 2009

Identification of plasma instability from wavelet spectra in a current disruption event

P. H. Yoon,[1] A. T. Y. Lui,[2] and J. W. Bonnell[3]

Received 13 October 2008; revised 5 January 2009; accepted 2 February 2009; published 18 April 2009.

[1] We investigate the plasma instability of a current disruption event that shows an inverse cascade of waves starting at frequencies slightly below the ion cyclotron frequency to waves at low frequencies that correspond to the time scale of dipolarization. The electric and magnetic perturbations in the initial wave excited are extracted to check their agreement with two alternative theoretically predicted instability mechanisms. The first mechanism involves the electromagnetic ion cyclotron instability propagating along the magnetic field driven by the relative cross-field drift, while the second corresponds to the Alfvén ion cyclotron instability propagating in quasi-perpendicular direction with respect to the local magnetic field. It is found that the observed electric and magnetic perturbations are incompatible with the quasi-parallel electromagnetic ion cyclotron instability, but they are found to be consistent with nearly perpendicular propagating waves generated by the Alfvén ion cyclotron instability.

Citation: Yoon, P. H., A. T. Y. Lui, and J. W. Bonnell (2009), Identification of plasma instability from wavelet spectra in a current disruption event, *J. Geophys. Res.*, *114*, A04207, doi:10.1029/2008JA013816.

1. Introduction

[2] The interaction between the solar wind and the Earth's magnetic field leads to the formation of the magnetosphere. Its volume is conservatively estimated to exceed ten thousand times the size of the Earth. Many different plasma domains exist within the magnetosphere. The magnetic field intensity, plasma temperature, and the plasma density vary considerably among these different regimes. These variations give rise to a wide range of key plasma parameters for consideration when basic physical processes are sought for the origin of different magnetospheric phenomena.

[3] Magnetospheric substorms constitute a major challenge in understanding such a phenomenon that involves an explosive energy release at its onset. As a first step to unravel the physical process for its onset, the recent NASA mission Time History of Events and Macroscale Interactions during Substorms (THEMIS) aims to identify the location where the substorm disturbances are initiated in the magnetotail [*Angelopoulos*, 2008]. The result from this first step will confine the range of plasma parameters appropriate for the identification of the substorm onset process. Regardless of where substorm onset occurs in the magnetotail, one phenomenon inevitably linked to the substorm disturbances in the magnetotail is dipolarization, which is a reconfiguration of the magnetic field from a tail-like form consisting of much magnetic tension to a less stressed dipolar form.

[4] There are several potential causes of dipolarization. The process that relates directly to magnetic reconnection is the braking of the reconnection-generated plasma flows in the near-Earth region due to the strong magnetic field [*Haerendel*, 1992; *Shiokawa et al.*, 1997]. Near-Earth processes for dipolarization include plasma instabilities and noninstability type. In the first category are ballooning instability [*Roux et al.*, 1991; *Voronkov et al.*, 1997; *Liu*, 1997; *Bhattacharjee et al.*, 1998; *Cheng and Lui*, 1998; *Pu et al.*, 1999; *Erickson et al.*, 2000; *Dobias et al.*, 2004], cross-field current instability [*Lui et al.*, 1991], entropy antidiffusion instability [*Lee et al.*, 1998], current-driven Alfvénic instability [*Perraut et al.*, 2000; *Le Contel et al.*, 2001], and ion-ion two stream instability [*Swift and Lin*, 2001]. The second category includes convection reduction [*Lyons et al.*, 2003], magnetosphere-ionosphere coupling [*Kan*, 2007], and "akis" structure in a thin current sheet [*Sarafopoulos*, 2008].

[5] In a recent study of such dipolarization phenomenon, *Lui et al.* [2008a] showed from continuous wavelet analysis of the magnetic field signals that current disruption in one dipolarization event exhibits a clear inverse cascade feature of waves starting at frequencies slightly below the ion cyclotron frequency to waves at low frequencies that correspond to the time scale of dipolarization. A preliminary theoretical analysis was made to suggest that the initial waves in the inverse cascade feature might be due to drift-driven electromagnetic ion cyclotron instability or an ordinary mode instability driven by a cross-field ion drift. This early effort was made without the knowledge of the accompanying electric field fluctuations. After the completion of this previous work, we were able to examine the associated electric perturbations at the onset of the inverse cascade feature. The additional information allows us to

[1] IPST, University of Maryland, College Park, Maryland, USA.
[2] Johns Hopkins University Applied Physics Laboratory, Laurel, Maryland, USA.
[3] Space Sciences Laboratory, University of California, Berkeley, California, USA.

0148-0227/09/2008JA013816$09.00

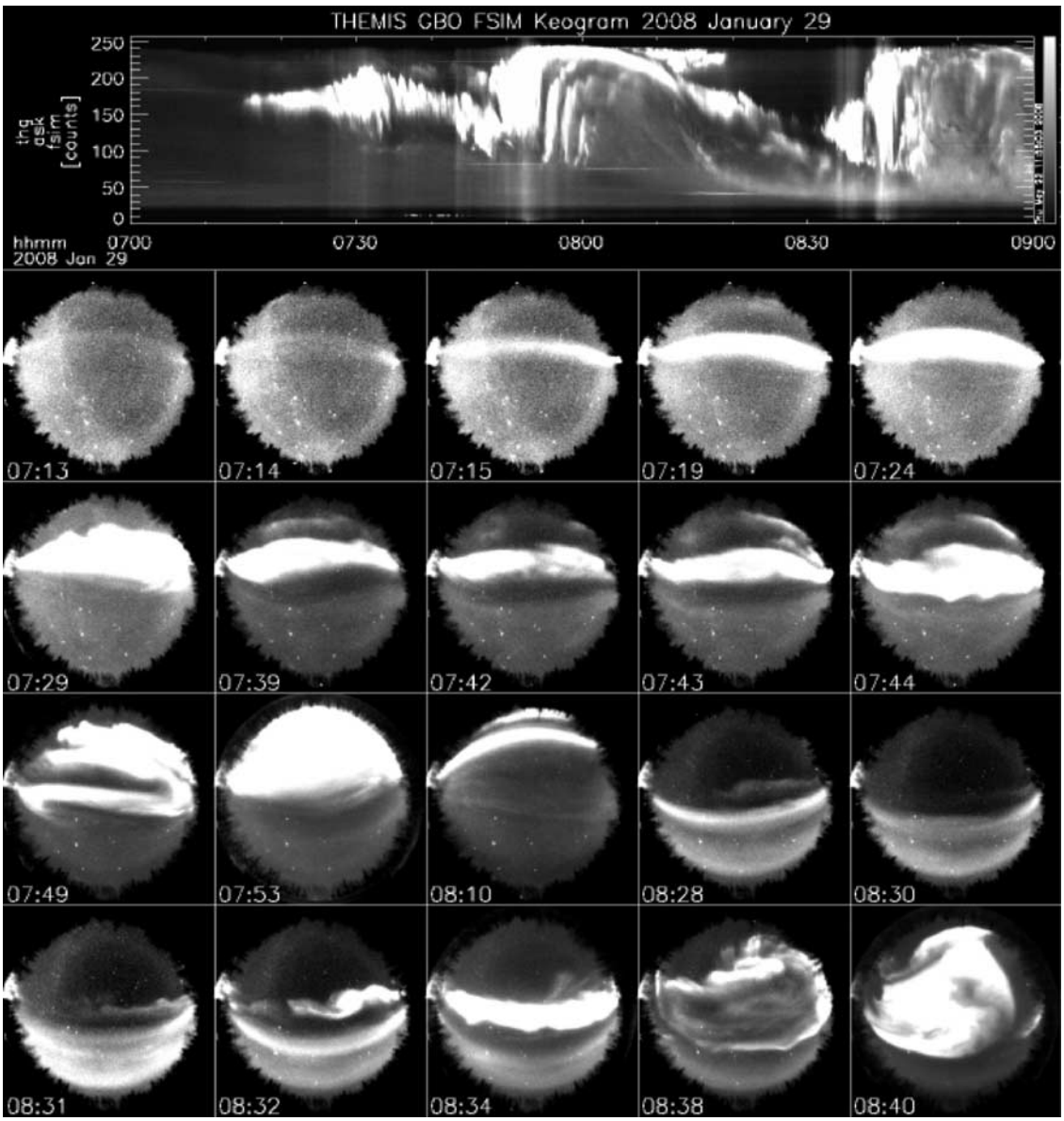

Figure 1. The keogram and selected 1-min resolution of ASC auroral images from Fort Smith during 0700–0900 UT on 29 January 2008.

better identify the instability that was excited at the abrupt onset of dipolarization.

[6] In this paper, we shall first present the magnetic and electric perturbations observed during the dipolarization event. We then present a theoretical procedure to ascertain the nature of the excited waves that allows us to identify the instability that might cause the observed magnetic and electric perturbations at dipolarization.

2. Observations

[7] A moderate-sized substorm started at ~0743 UT on 29 January 2008 and was monitored well by both the ground-based all-sky-camera observatories [*Mende et al.*, 2008] and the THEMIS satellites [*Angelopoulos*, 2008]. Figure 1 shows the keogram from Fort Smith (FSMI), located at geog. Lat. = 59.984N, geog. Long. = 248.158E, and selected frames of 1-min resolution auroral picture from the all-sky-camera (ASC) on that day [*Lui et al.*, 2008b]. As is well known, keogram represents the auroral brightness along the north-south meridian as a function of time. A weak substorm can be seen to start at ~0713 UT, preceding the moderate-sized substorm that started later at ~0743 UT. The second substorm within this time interval had a significant poleward expansion of auroral activity, as indicated by the keogram as well as pictures taken at 0749–0810 UT in the sequence shown. The keogram indicates that the poleward boundary of auroral activity within the field of view of that station started to recede at ~0820 UT.

[8] Dipolarization was observed by the innermost THEMIS satellite, which was located at $(X, Y, Z)_{GSM}$ = $(-8.3, 1.3, -2.7)R_E$ in the magnetotail. Figure 2 shows the measurements of the electric and magnetic fields during the short interval encompassing the dipolarization. The electric

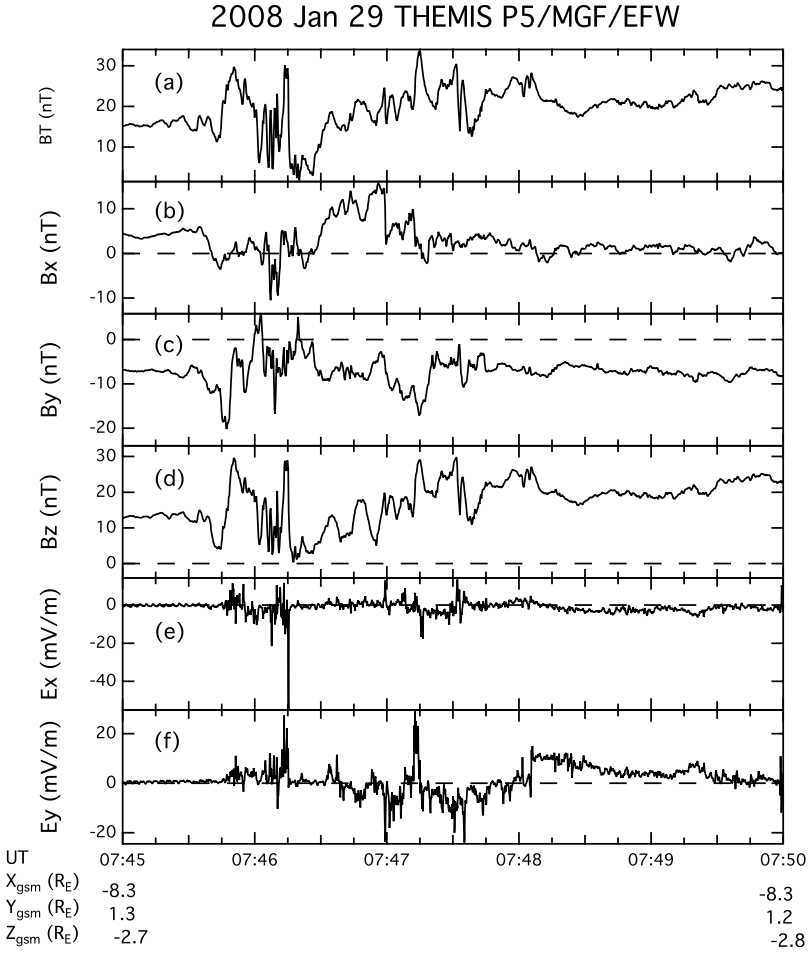

Figure 2. (a–d) The three components of magnetic field and (e and f) two components of electric field measured by innermost probe of the THEMIS A (P5) during the short interval encompassing the current disruption.

field data are from the Electric Field Instrument (EFI) [*Bonnell et al.*, 2008] and the magnetic field data are from the FluxGate Magnetometer (FGM) [*Auster et al.*, 2008]. The electric field components are obtained using the approximation of $\mathbf{E} \cdot \mathbf{B} = 0$. Only the two electric field components on the equatorial plane are shown since the third component is mostly contributed from the short axial boom and has less accuracy than the other two components.

[9] Continuous wavelet transform using the Gaussian Morlet mother wavelet as documented by *Lui and Najmi* [1997] is used to examine the magnetic and electric field perturbations associated with dipolarization for this event. Wavelet analysis uses wavelet packets to resolve the observed signal in a time-frequency domain, which is superior to the traditional Fourier analysis [*Lui and Najmi*, 1997; *Lui et al.*, 2008a]. The Gaussian width of the envelope is chosen to be 0.5 and the frequency domain is divided into 8 octaves, each with 15 divisions. The temporal resolution of the magnetic field data is 0.25 s and that of the electric field is 0.125 s. Figures 3 and 4 show the wavelet analysis for the magnetic field and electric field components, respectively. The local proton cyclotron frequency is marked by the white trace in each frequency-time spectrogram. For magnetic field perturbations, the inverse cascade feature can be seen in the B_y and B_z components during the early phase of current disruption (~0746–0748 UT). The B_z component showed this feature most evidently. The inverse cascade began at the high frequencies around ~0.1 Hz and settled at the low frequencies of ~0.005–0.009 Hz. The time scale of dipolarization for this activity was ~150 s (0745:40–0748:10 UT), which corresponds to ~0.007 Hz. For the electric field perturbations, there is some indication of an inverse cascade in the E_y component in the interval ~0747–0748 UT also. It started at the high frequencies around ~0.1 Hz and descended to the low frequencies at ~0.005–0.009 Hz, just like that of the Bz component but occurred at a different time interval. In the present analysis the frequency separation is gained with the wavelet analysis, and the accuracy of the perturbed magnetic field components is better than 1 nT.

3. Plasma Wave Diagnostics

[10] In this section, we outline the theoretical diagnostic tool which will be utilized for data analysis. The purpose of the formalism is to identify and characterize the nature of the fluctuation. The spacecraft measurement is done for a given range of frequencies, whereas the characteristics of

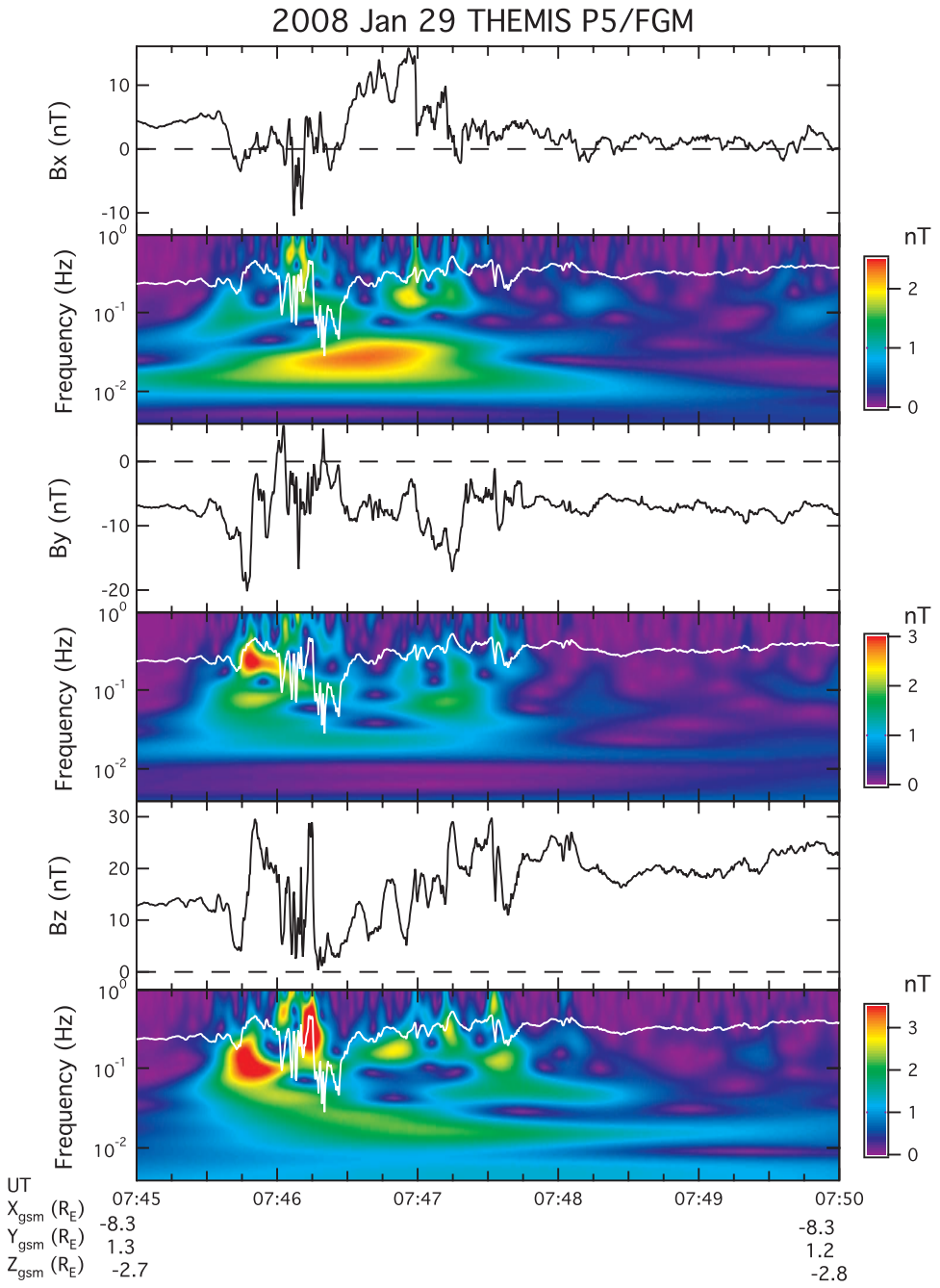

Figure 3. The wavelet analysis result on all three magnetic field components showing the inverse cascade feature and intermittent excitations.

the plasma eigenmode can be described in terms of frequency, propagation angle, and the wave polarization. Of these, the information on the propagation angle is not available directly. The data provides electric and magnetic field fluctuations, but the interpretation of the wave electric and magnetic field must be done within the context of the plasma normal mode theory. The theoretical scheme to be discussed below is a tool that enables us to extract the necessary information, namely, the propagation angle and the wave polarization so that we may unambiguously identify the nature of the fluctuations.

[11] Consider the linearized two-fluid equation in magnetized plasmas with an arbitrary orientation of the ambient magnetic field,

$$\delta n_j = \frac{n\mathbf{k}\cdot\delta\mathbf{v}_j}{\omega},$$
$$\delta\mathbf{v}_j = \frac{ie_j}{m_j\omega}\,\delta\mathbf{E} - \frac{ie_j}{m_jc\omega}\,\mathbf{B}\times\delta\mathbf{v}_j,$$
$$\delta\mathbf{B} = \frac{c}{\omega}\mathbf{k}\times\delta\mathbf{E},$$
$$\delta\mathbf{E} + \frac{c}{\omega}\,\mathbf{k}\times\delta\mathbf{B} = -\sum_j \frac{4\pi ie_jn}{\omega}\,\delta\mathbf{v}_j,$$

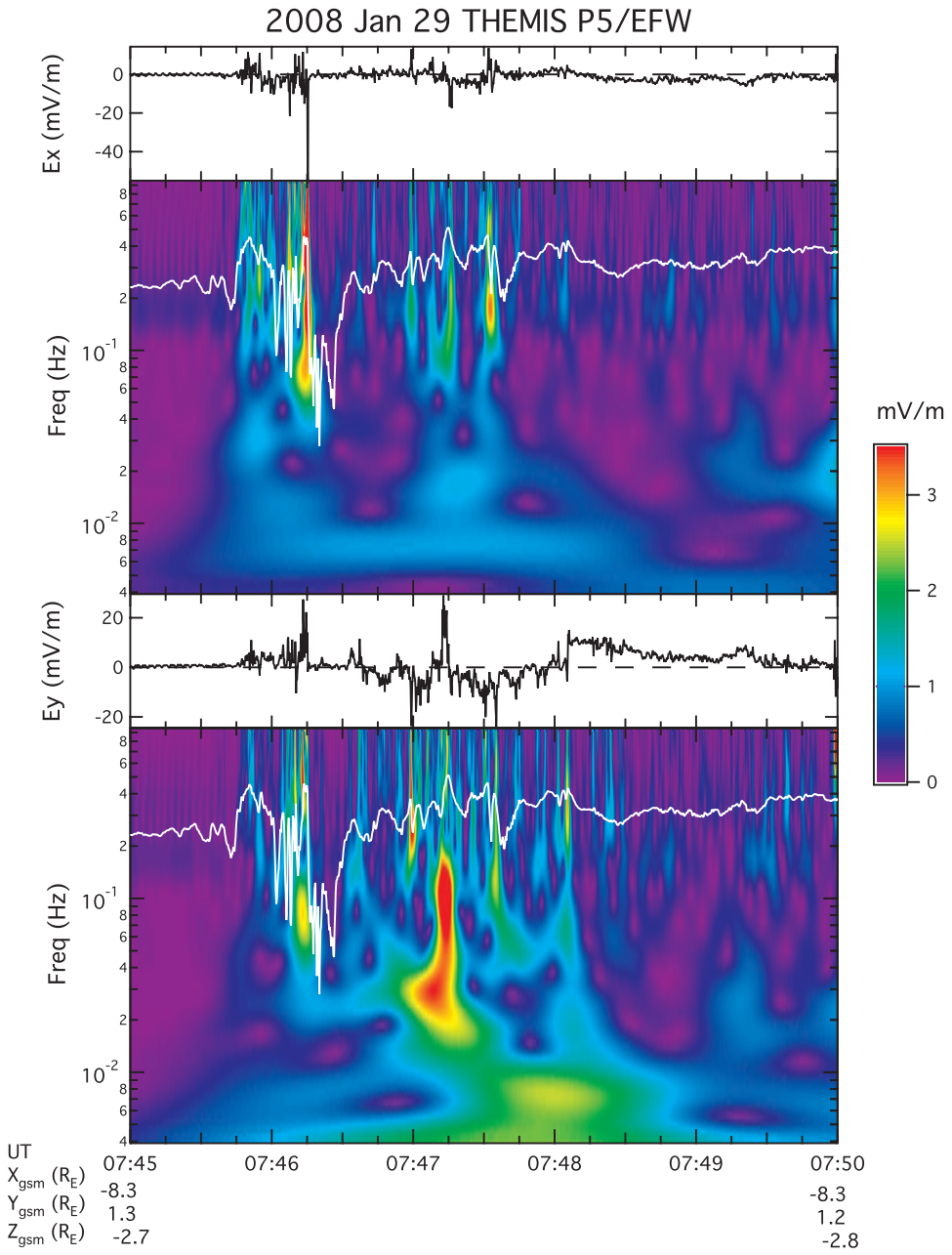

Figure 4. The wavelet analysis result on two electric field components showing an indication of an inverse cascade feature and intermittent excitations.

where δn_j and $\delta \mathbf{v}_j$ stand for perturbed number density and velocity for particle species j ($j = e$, i being electron and ions, respectively), $\delta \mathbf{E}$ and $\delta \mathbf{B}$ are fluctuating electric and magnetic fields, and B stands for the ambient magnetic field. Moreover, e_j, m_j, and c designate the unit electric charge, mass, and the speed of light in vacuo. The above linearized two-fluid equations can be combined to give the following wave equation:

$$0 = \left(1 - \frac{c^2 k^2}{\omega^2} - \sum_j \frac{\omega_{pj}^2}{\omega^2 - \Omega_j^2}\right) \delta \mathbf{E} + \frac{c^2}{\omega^2} (\mathbf{k} \cdot \delta \mathbf{E}) \mathbf{k} + \sum_j \frac{\omega_{pj}^2}{\omega^2 - \Omega_j^2} \left(\frac{\Omega_j^2}{\omega^2} (\mathbf{b} \cdot \delta \mathbf{E}) \mathbf{b} + \frac{i \Omega_j}{\omega} (\mathbf{b} \times \delta \mathbf{E})\right), \quad (1)$$

where $\omega_{pj}^2 = 4\pi n e_j^2 / m_j$ corresponds to the square of the plasma frequency for species j, and $\Omega_j = e_j B / m_j c$ denotes the cyclotron frequency for species j. In the above, $\mathbf{b} = \mathbf{B}/|\mathbf{B}|$ stands for unit magnetic field vector.

3.1. Dispersion Relation for Low-Frequency Modes

[12] The solvability condition of the above equation, or the dispersion relation, is well known. If we decompose the wave vector $\mathbf{k}$ into components perpendicular and parallel to the ambient field,

$$\mathbf{k} = (\mathbf{b} \times \mathbf{k}) \times \mathbf{b} + (\mathbf{b} \cdot \mathbf{k}) \mathbf{b} = \mathbf{k}_\perp + \mathbf{k}_\parallel,$$

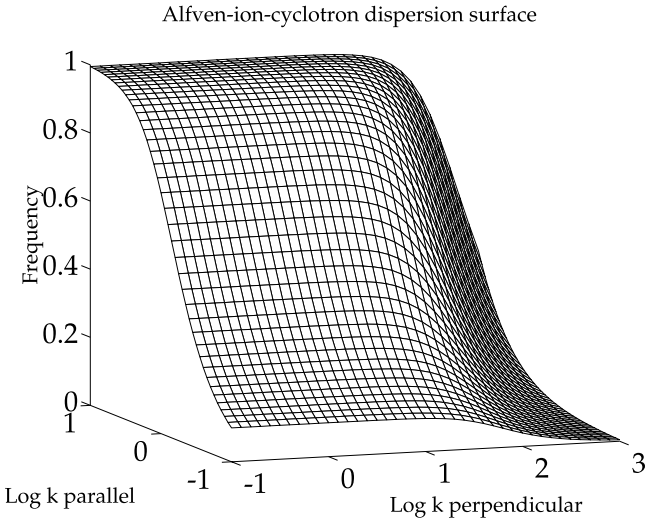

Figure 5a. Dispersion surface for Alfvén ion cyclotron mode, which is one of the two linearly independent low-frequency modes in magnetized plasmas. The frequency is normalized to ω/Ω_i, and the wave vector is normalized by $\mathbf{k}v_A/\Omega_i$.

then the dispersion relation is given by

$$0 = N^4\left(\epsilon_1 \sin^2\theta + \epsilon_3 \cos^2\theta\right) - N^2\left[\left(\epsilon_1^2+\epsilon_2^2\right)\sin^2\theta + \epsilon_1\epsilon_3\left(1+\cos^2\theta\right)\right] + \left(\epsilon_1^2+\epsilon_2^2\right)\epsilon_3,$$

where $N = ck/\omega$ is the index of refraction, $k_\perp = k\sin\theta$, $k_\parallel = k\cos\theta$, and

$$\epsilon_1 = 1 - \sum_j \frac{\omega_{pj}^2}{\omega^2-\Omega_j^2},$$
$$\epsilon_2 = \sum_j \frac{i\Omega_j}{\omega}\frac{\omega_{pj}^2}{\omega^2-\Omega_j^2},$$
$$\epsilon_3 = 1 - \sum_j \frac{\omega_{pj}^2}{\omega^2}.$$

For low-frequency waves satisfying $\omega^2 \ll \Omega_e^2$, we may approximate

$$\epsilon_1 = \frac{\omega_{pi}^2}{\omega_{lh}^2} - \frac{\omega_{pi}^2}{\omega^2-\Omega_i^2},$$
$$\epsilon_2 = \frac{i\omega}{\Omega_i}\frac{\omega_{pi}^2}{\omega^2-\Omega_i^2},$$
$$\epsilon_3 = -\frac{\omega_{pe}^2}{\omega^2}.$$

In the above $\omega_{lh}^2 = \Omega_i^2(m_i/m_e)$ is the square of the lower-hybrid frequency. Under the above approximations, the dispersion relation can be expressed as a quadratic equation in ω^2,

$$0 = A\frac{\omega^4}{\Omega_i^4} - B\frac{\omega^2}{\Omega_i^2} + C,$$

where

$$A = 1 + \frac{2k^2v_A^2}{\omega_{lh}^2} + \frac{k^2k_\perp^2v_A^4}{\omega_{lh}^4},$$
$$B = \frac{k^2k_\parallel^2v_A^4}{\Omega_i^4} + \frac{k^2v_A^2}{\omega_{lh}^2}\frac{k_\perp^2v_A^2}{\Omega_i^2} + \frac{k^2v_A^2}{\Omega_i^2} + \frac{k_\parallel^2v_A^2}{\Omega_i^2},$$
$$C = \frac{k^2k_\parallel^2v_A^4}{\Omega_i^4}.$$

Here $v_A = B/\sqrt{4\pi n m_i}$ is the Alfvén speed. Of course, the exact solution is available, but to a good degree of accurateness, one may obtain the following approximate analytical forms for the two independent solutions,

$$\frac{\omega}{\Omega_i} \approx \left(\frac{C}{B}\right)^{1/2} = \frac{k_\parallel v_A/\Omega_i}{\sqrt{1+k_\parallel^2v_A^2/\Omega_i^2 + k_\perp^2v_A^2/\omega_{lh}^2}},$$
$$\frac{\omega}{\Omega_i} \approx \left(\frac{B}{A}\right)^{1/2} = \frac{kv_A}{\Omega_i}\sqrt{\frac{1+k_\parallel^2v_A^2/\Omega_i^2 + k_\perp^2v_A^2/\omega_{lh}^2}{1+2k^2v_A^2/\omega_{lh}^2 + k^2k_\perp^2v_A^4/\omega_{lh}^4}}. \quad (2)$$

The first solution corresponds to the Alfvén ion cyclotron mode branch, while the second solution describes dispersive property of the fast magnetosonic mode branch.

[13] Shown in Figures 5a and 5b are the surface plots of the above two linearly independent low-frequency plasma eigenmodes. Note that the ion cyclotron mode does not exist above Ω_i. For quasi-perpendicular propagation angle, this mode can be described by the O mode polarization. The fast magnetosonic mode can have wave frequency much higher than Ω_i. For quasi-perpendicular propagation angle, the fast mode turns into quasi-electrostatic lower-hybrid wave.

3.2. Wave Polarization

[14] In what follows, we first start from the consideration of the situation where the ambient magnetic field is directed

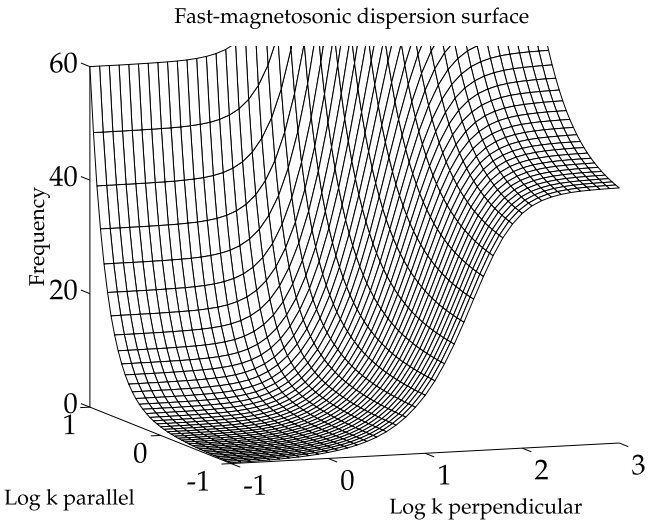

Figure 5b. Dispersion surface for fast magnetosonic mode, which is the second solution among the two linearly independent low-frequency modes in magnetized plasmas. The frequency is normalized to ω/Ω_i, and the wave vector is normalized by $\mathbf{k}v_A/\Omega_i$.

strictly along the z axis, and consider the wave vector to lie in yz plane,

$$\mathbf{B} = B\mathbf{e}_z,$$
$$\mathbf{k} = k_\perp \mathbf{e}_y + k_\parallel \mathbf{e}_z = k\sin\theta\,\mathbf{e}_y + k\cos\theta\,\mathbf{e}_z.$$

However, this is not the most general geometry. Consequently, we next allow the ambient magnetic field to possess a finite y component. To do that, we simply rotate the geometry of **B** and **k** vectors in clockwise direction about x axis in angle α. The new **B** and **k** vectors are then given by

$$\mathbf{B} = B\sin\alpha\,\mathbf{e}_y + B\cos\alpha\,\mathbf{e}_z,$$
$$\mathbf{k} = k\sin(\theta+\alpha)\,\mathbf{e}_y + k\cos(\theta+\alpha)\,\mathbf{e}_z.$$

Finally, in order to allow a finite x component magnetic field, we rotate the above **B** and **k** vectors in counterclockwise direction about y axis in angle β. The result is

$$\mathbf{B} = B\cos\alpha\sin\beta\,\mathbf{e}_x + B\sin\alpha\,\mathbf{e}_y + B\cos\alpha\cos\beta\,\mathbf{e}_z,$$
$$\mathbf{k} = k\cos(\theta+\alpha)\sin\beta\,\mathbf{e}_x + k\sin(\theta+\alpha)\,\mathbf{e}_y + k\cos(\theta+\alpha)\cos\beta\,\mathbf{e}_z.$$

By identifying

$$b_x = \cos\alpha\sin\beta,$$
$$b_y = \sin\alpha,$$
$$b_z = \cos\alpha\cos\beta,$$

we may easily reexpress the **k** vector as follows:

$$\mathbf{k} = \mathbf{e}_x k_x + \mathbf{e}_y k_y + \mathbf{e}_z k_z,$$
$$k_x = kb_x\left(\cos\theta - \frac{b_y}{\sqrt{1-b_y^2}}\sin\theta\right),$$
$$k_y = k\left(\sqrt{1-b_y^2}\sin\theta + b_y\cos\theta\right),$$
$$k_z = kb_z\left(\cos\theta - \frac{b_y}{\sqrt{1-b_y^2}}\sin\theta\right).$$

[15] Now that we have obtained the general expressions for both **B** and **k** vectors, we go back to the wave equation (1). After some tedious but otherwise straightforward algebraic manipulations, one may express five out of the six electric and magnetic field components in terms of one undetermined component. We choose δE_z as the undetermined element. Then, it can be shown that

$$\begin{aligned}
\frac{\delta E_x}{\delta E_z} &= \frac{P}{R},\\
\frac{\delta E_y}{\delta E_z} &= \frac{Q}{R},\\
\frac{\delta B_x}{\delta E_z} &= \frac{c}{v_A}\frac{\Omega_i}{\omega}\left(\frac{k_y v_A}{\Omega_i} - \frac{k_z v_A}{\Omega_i}\frac{Q}{R}\right),\\
\frac{\delta B_y}{\delta E_z} &= -\frac{c}{v_A}\frac{\Omega_i}{\omega}\left(\frac{k_x v_A}{\Omega_i} - \frac{k_z v_A}{\Omega_i}\frac{P}{R}\right),\\
\frac{\delta B_z}{\delta E_z} &= \frac{c}{v_A}\frac{\Omega_i}{\omega}\left(\frac{k_x v_A}{\Omega_i}\frac{Q}{R} - \frac{k_y v_A}{\Omega_i}\frac{P}{R}\right),
\end{aligned} \tag{3}$$

where

$$\begin{aligned}
P &= D_{xy}D_{yz} + D_{yy}D_{xz},\\
Q &= D_{xy}D_{xz} + D_{xx}D_{yz},\\
R &= D_{xx}D_{yy} - D_{xy}^2,\\
D_{xx} &= \left(\frac{k_y^2 v_A^2}{\Omega_i^2} + \frac{k_z^2 v_A^2}{\Omega_i^2} - \frac{\omega^2}{\omega_{lh}^2} + \frac{m_i}{m_e}b_x^2\right)\left(1 - \frac{\omega^2}{\Omega_i^2}\right) - \frac{\omega^2}{\Omega_i^2} + b_x^2,\\
D_{yy} &= \left(\frac{k_x^2 v_A^2}{\Omega_i^2} + \frac{k_z^2 v_A^2}{\Omega_i^2} - \frac{\omega^2}{\omega_{lh}^2} + \frac{m_i}{m_e}b_y^2\right)\left(1 - \frac{\omega^2}{\Omega_i^2}\right) - \frac{\omega^2}{\Omega_i^2} + b_y^2,\\
D_{xy} &= \left(\frac{k_x k_y v_A^2}{\Omega_i^2} + \frac{i\omega}{\Omega_i}b_z - \frac{m_i}{m_e}b_x b_y\right)\left(1 - \frac{\omega^2}{\Omega_i^2}\right) - \frac{i\omega}{\Omega_i}b_z - b_x b_y,\\
D_{xz} &= \left(\frac{k_x k_z v_A^2}{\Omega_i^2} + \frac{i\omega}{\Omega_i}b_y - \frac{m_i}{m_e}b_x b_z\right)\left(1 - \frac{\omega^2}{\Omega_i^2}\right) - \frac{i\omega}{\Omega_i}b_y - b_x b_z,\\
D_{yz} &= \left(\frac{k_y k_z v_A^2}{\Omega_i^2} + \frac{i\omega}{\Omega_i}b_x - \frac{m_i}{m_e}b_y b_z\right)\left(1 - \frac{\omega^2}{\Omega_i^2}\right) + \frac{i\omega}{\Omega_i}b_x - b_y b_z.
\end{aligned} \tag{4}$$

In the above the angular frequency ω and the wave vector **k** are not independent but they are mutually related via the dispersion relation (2).

[16] For the present purpose, instead of expressing ω in terms of **k**, we find it more useful to expression the magnitude of the wave vector k in terms of the frequency ω and the propagation angle θ. One can convert the dispersion relation (2) in a straightforward manner, and the result is

$$k^2 v_A^2 = \frac{\left(\omega_{\max}^A\right)^2}{\cos^2\theta}\frac{\omega^2}{\left(\omega_{\max}^A\right)^2 - \omega^2},$$
$$\left(\omega_{\max}^A\right)^2 = \cos^2\theta\,\frac{\Omega_i^2}{\cos^2\theta + \left(\Omega_i/\omega_{lh}\right)^2\sin^2\theta}, \tag{5}$$

for the Alfvén ion cyclotron mode branch, and

$$k^2 v_A^2 = \frac{\omega_{lh}^2}{2\sin^2\theta}\frac{2\omega^2 - \omega_{lh}^2 + \omega_{lh}^2\sqrt{1 + 2(\omega/\omega_{lh})^2 + 4(\omega/\Omega_i)^2\left(1 + \omega^2/\Omega_i^2\right)\cos^2\theta}}{\left(\omega_{\max}^F\right)^2 - \omega^2},$$
$$\left(\omega_{\max}^F\right)^2 = \omega_{lh}^2\,\frac{\sin^2\theta + (\omega_{lh}/\Omega_i)^2\cos^2\theta}{\sin^2\theta}, \tag{6}$$

for the fast magnetosonic mode branch. Shown in Figures 6a and 6b are the two solutions (5) and (6) plotted as normalized

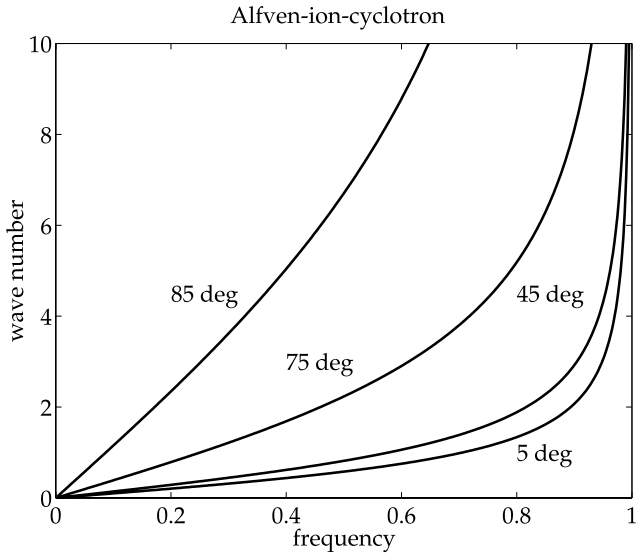

Figure 6a. Dispersion relation for Alfvén ion cyclotron mode expressed as k versus ω for several different propagation angles θ.

k versus normalized ω for several different propagation angles θ.

[17] We next make use of the results derived in this section to analyze the data. Our purpose is to identify the wave propagation angle defined with respect to the local magnetic field, and to determine which of the two linear independent modes is excited during the dipolarization process.

3.3. Data Analysis

[18] At the first time of interest, 0745:50 UT, corresponding close to the start of current disruption and inverse cascade feature, the parameters extracted are summarized in Table 1. For this event, we have chosen three discrete

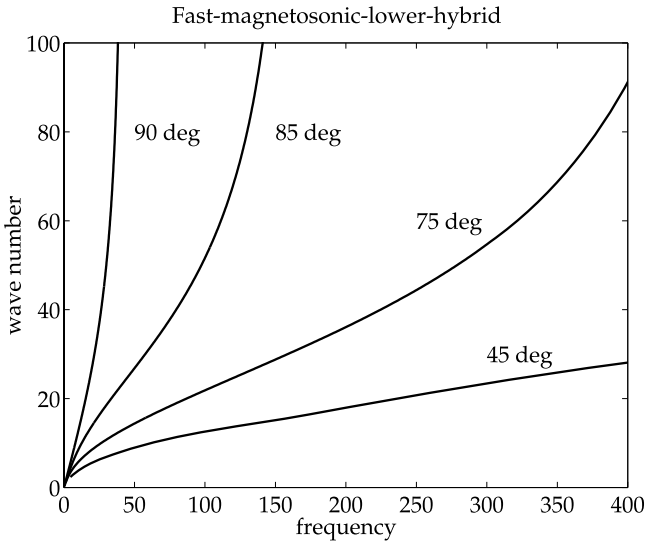

Figure 6b. Dispersion relations for fast magnetosonic mode expressed as k versus ω for several different propagation angles θ.

Table 1. Summary of Relevant Input Parameters for Event 1 at 0745:50 UT[a]

f_w (Hz)	δB_x (nT)	δB_y (nT)	δB_z (nT)	δE_x (mV/m)	δE_y (mV/m)
0.0947	1.1663	1.8201	3.8327	1.0364	0.2385
0.0947	1.1623	1.8177	3.8359	1.0221	0.2420
0.0947	1.1585	1.8152	3.8377	1.0062	0.2263
0.0992	1.1034	1.6632	3.8497	1.1051	0.1982
0.0992	1.0988	1.6565	3.8506	1.0922	0.1990
0.0992	1.0944	1.6498	3.8501	1.0778	0.2008
0.1031	1.0178	1.5005	3.8368	1.1660	0.1623
0.1031	1.0117	1.4875	3.8339	1.1541	0.1592
0.1031	1.0059	1.4747	3.8294	1.1404	0.1573

[a]For this event, f_{ci} = 0.4268 Hz, v_A = 801.1 km/s, B_x = 0.6 nT, B_y = −4.4 nT, and B_z = 27.7 nT.

frequency intervals corresponding to 0.0947 Hz, 0.0992 Hz, and 0.1031 Hz. We have then extracted the fluctuating field values for each frequency. We have used three adjacent data for each frequency interval for statistical average. The three frequency intervals can be translated as ω/Ω_i = 0.2219, 0.2324, and 0.2416, respectively. The unit magnetic field vector for this event is given by **b** = (0.0214, −0.1568, 0.9874).

[19] From Table 1, average values of ($\delta B_x/\delta B_z$, $\delta B_y/\delta B_z$, $\delta E_x/\delta E_y$) are given by (∼0.3, ∼0.5, ∼4.2) for ω/Ω_i = 0.2219; (∼0.3, ∼0.4, ∼5.5) for ω/Ω_i = 0.2324; and (∼0.3, ∼0.4, ∼7.3) for ω/Ω_i = 0.2416. We then compare the theoretically computed values on the basis of (3) and (4) with the above values for each mode (5) or (6). If the following quantities

$$\left.\frac{\delta B_x}{\delta B_z}\right|_{\text{theory}} - \left.\frac{\delta B_x}{\delta B_z}\right|_{\text{data}},$$
$$\left.\frac{\delta B_y}{\delta B_z}\right|_{\text{theory}} - \left.\frac{\delta B_y}{\delta B_z}\right|_{\text{data}},$$
$$\left.\frac{\delta E_x}{\delta E_y}\right|_{\text{theory}} - \left.\frac{\delta E_x}{\delta E_y}\right|_{\text{data}}, \tag{7}$$

should approach zero value simultaneously for a given propagation angle θ, then obviously that angle characterizes the excited wave mode. We have computed the above quantities for all three frequency intervals. It turns out that the fast magnetosonic mode does not render the above three quantities simultaneously to zero for any propagation angle. Consequently, we do not show the results of our investigation related to the fast magnetosonic mode.

[20] The Alfvén ion cyclotron branch on the other hand shows that the above three quantities simultaneously tend toward zero value for a particular propagation angle θ. Shown in Figures 7a, 7b, and 7c are the results for the Alfvén ion cyclotron wave polarization study. Although exact zero values are not achieved owing to the inherent uncertainty in the data and the fact that the theory (specifically, we upshifted both curves $(\delta B_x/\delta B_z)_{\text{theory}} - (\delta B_x/\delta B_z)_{\text{data}}$ and $(\delta B_y/\delta B_z)_{\text{theory}} - (\delta B_y/\delta B_z)_{\text{data}}$ by 0.075) is based upon simple cold two-fluid theory, the overall trend is clear enough so that we may confidently declare that the root (i.e., the propagation angle) has been found for each angle. Specifically, we find that the quantities defined in (7) simultaneously approach zero value for $\theta \approx 80°$, 79.5°, and 79°, for the three frequency intervals. Note that we did not adjust $(\delta E_x/\delta E_y)_{\text{theory}} - (\delta E_x/\delta E_y)_{\text{data}}$.

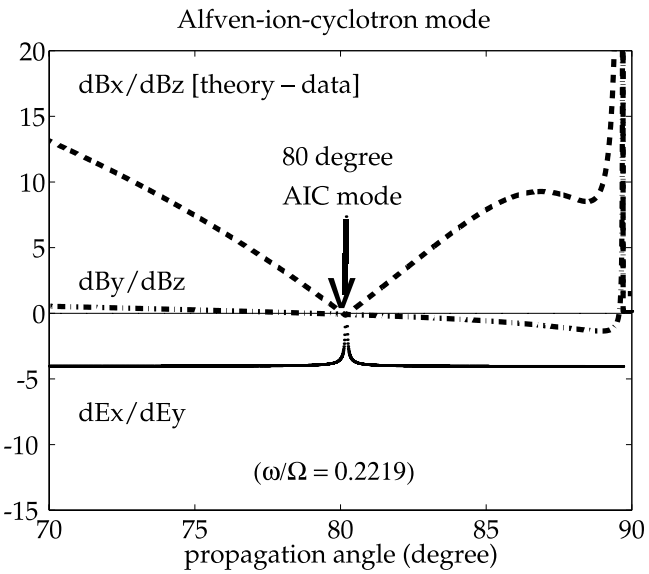

Figure 7a. Plots of $(\delta B_x/\delta B_z)_{\text{theory}} - (\delta B_x/\delta B_z)_{\text{data}}$ (top curve), $(\delta B_y/\delta B_z)_{\text{theory}} - (\delta B_y/\delta B_z)_{\text{data}}$ (middle curve), and $(\delta E_x/\delta E_y)_{\text{theory}} - (\delta E_x/\delta E_y)_{\text{data}}$ (bottom curve) corresponding to the Alfvén ion cyclotron branch for $\omega/\Omega_i = 0.2219$. Note that the fast mode does not have a solution.

[21] The Alfvén ion cyclotron mode for quasi-perpendicular propagation is characterized by the ordinary mode polarization. The k versus ω dispersion relation for the three angles identified by the processes shown in Figures 7a, 7b, and 7c is plotted in Figure 8. Of the continuous dispersion relation, only the discrete frequencies indicated by short vertical lines represent the data points. In the paper by *Lui et al.* [2008a], we considered two possible unstable modes, one propagating exactly parallel to the local average magnetic field, and the other was the ordinary mode propagating exactly perpendicular to the ambient B field. Judging from the present analysis, we conclude that the latter O mode instability is probably the unstable mode excited during the dipolarization process.

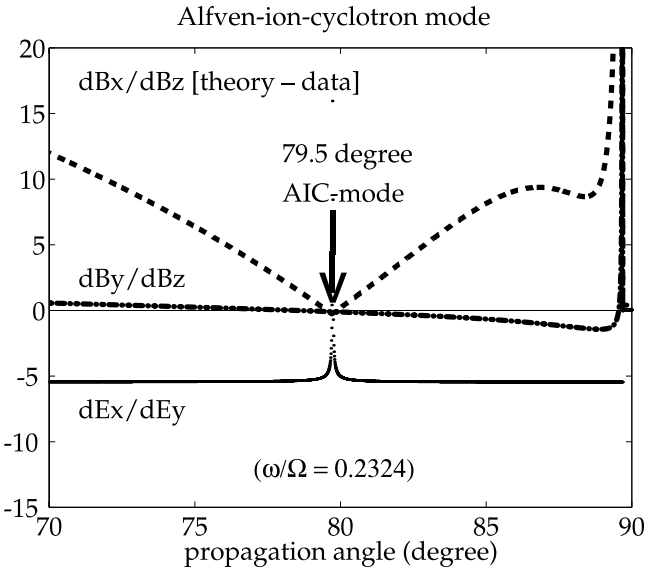

Figure 7b. The same as Figure 7a, but for $\omega/\Omega_i = 0.2324$.

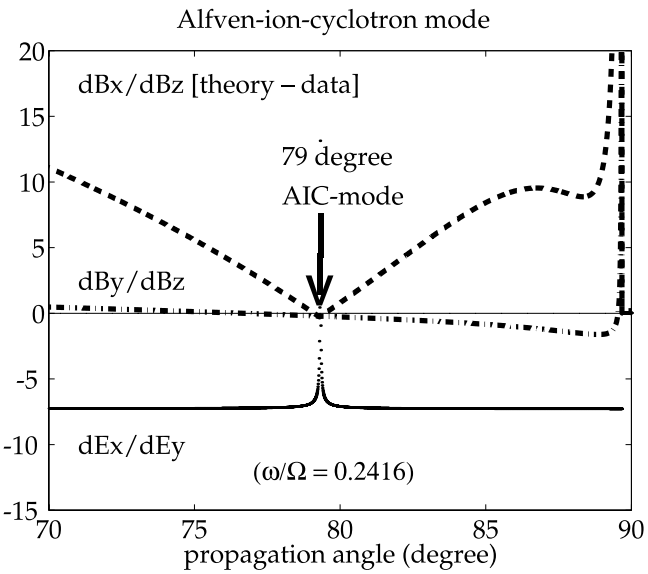

Figure 7c. The same as Figure 7a, but for $\omega/\Omega_i = 0.2416$.

[22] Next we consider another time of interest, 0747:14 UT. The parameters extracted are summarized in Table 2. We have again chosen three frequency intervals corresponding to 0.0992 Hz, 0.1031 Hz, and 0.1088 Hz. The three adjacent field data points for each frequency interval are shown in Table 2. The three frequency intervals are translated as $\omega/\Omega_i = 0.2013$, 0.2093, and 0.2208, respectively. The unit magnetic field vector for this event is given by $\mathbf{b} = (-0.0679, -0.4877, 0.8704)$.

[23] Average values of $(\delta B_x/\delta B_z, \delta B_y/\delta B_z, \delta E_x/\delta E_y)$ for this event are given by ($\sim$1.3, $\sim$2.1, $\sim$0.4) for $\omega/\Omega_i = 0.2013$; ($\sim$1.4, $\sim$3.1, $\sim$0.4) for $\omega/\Omega_i = 0.2093$; and ($\sim$1.2, $\sim$1.5,

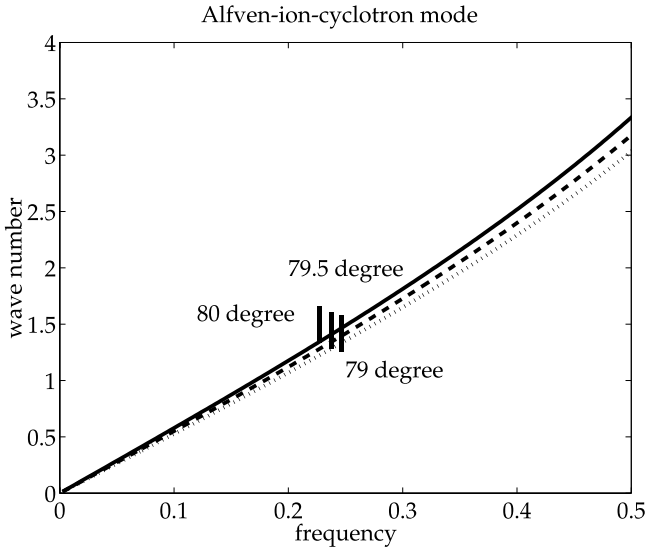

Figure 8. Alfvén ion cyclotron dispersion relation (k versus ω) for three angles: $\theta = 80°$ (top curve), 79.5° (middle curve), and 79° (bottom curve). The short vertical lines represent the data points. For these quasi-perpendicular propagation angles, the mode is characterized by the ordinary mode polarization.

Table 2. Summary of Relevant Input Parameters for Event 2 at 0747:14 UT[a]

f_w (Hz)	δB_x (nT)	δB_y (nT)	δB_z (nT)	δE_x (mV/m)	δE_y (mV/m)
0.0992	0.7810	1.3300	0.6373	1.9884	5.0301
0.0992	0.7922	1.3300	0.6337	2.0158	5.0330
0.0992	0.8027	1.3617	0.6291	2.0416	5.0278
0.1031	0.6321	1.4342	0.4754	2.0194	5.0155
0.1031	0.6457	1.4457	0.4684	2.0400	5.0194
0.1031	0.6584	1.4570	0.4607	2.0589	5.0152
0.1088	0.9332	1.2385	0.8218	1.9313	4.9903
0.1088	0.9418	1.2593	0.8203	1.9669	4.9921
0.1088	0.9497	1.2797	0.8178	2.0008	4.9860

[a]For this event, f_{ci} = 0.4927 Hz, v_A = 906.2 km/s, B_x = −2.2 nT, B_y = −15.8 nT, and B_z = 28.2 nT.

∼0.4) for ω/Ω_i = 0.2208. We have repeated the analysis of computing (7) as a function of propagation angle θ in order to determine whether these quantities approach zero value simultaneously for a given angle θ. Again, the fast magnetosonic mode does not satisfy the required condition. Consequently, we rule out the fast magnetosonic mode from the discussion. Figures 9a, 9b, and 9c show the results for Alfvén ion cyclotron polarization. We find that the quantities defined in (7) simultaneously approach zero value in an approximate sense, for $\theta \approx 87°$, 86.9°, and 86.7°, for the three frequency intervals. In this case, the vertical upshifts for the two curves $(\delta B_x/\delta B_z)_{\text{theory}} - (\delta B_x/\delta B_z)_{\text{data}}$ and $(\delta B_y/\delta B_z)_{\text{theory}} - (\delta B_y/\delta B_z)_{\text{data}}$ were about 1.

[24] Figure 10 shows the k versus ω dispersion relation for the three angles identified by the processes shown in Figures 9a, 9b, and 9c. The discrete frequencies representing the data points are indicated by short vertical lines. Again, the mode is quasi-perpendicular Alfvén ion cyclotron branch that is consistent with the O mode instability discussed in the paper by *Lui et al.* [2008a].

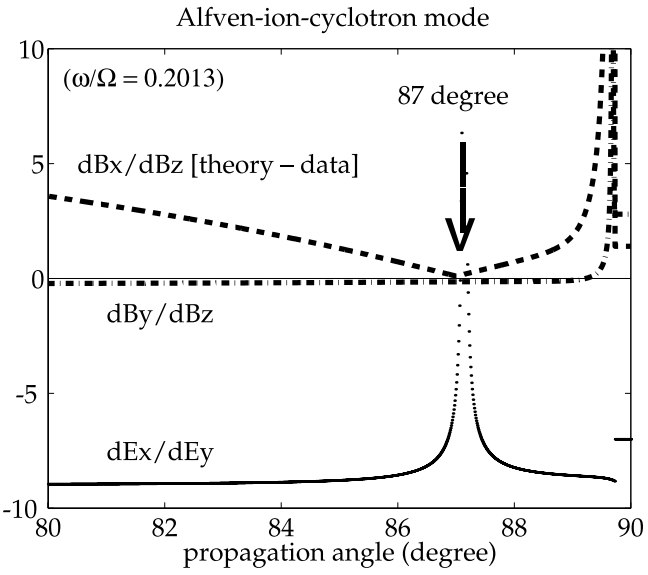

Figure 9a. Plots of $(\delta B_x/\delta B_z)_{\text{theory}} - (\delta B_x/\delta B_z)_{\text{data}}$ (top curve), $(\delta B_y/\delta B_z)_{\text{theory}} - (\delta B_y/\delta B_z)_{\text{data}}$ (middle curve), and $(\delta E_x/\delta E_y)_{\text{theory}} - (\delta E_x/\delta E_y)_{\text{data}}$ (bottom curve) corresponding to the Alfvén ion cyclotron branch for ω/Ω_i = 0.2013.

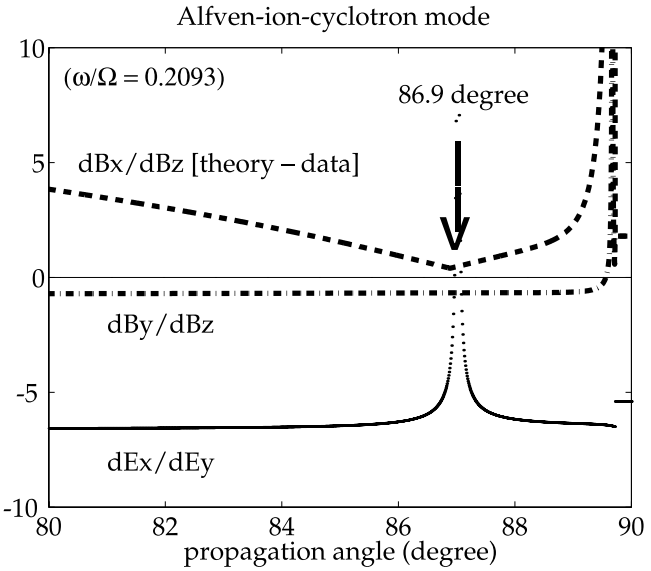

Figure 9b. The same Figure 9a, but for ω/Ω_i = 0.2093.

[25] Finally, we should mention that the average or bulk speed associated with the plasma along the direction of the wave propagation (i.e., quasi-perpendicular direction with respect to the local field) is negligible for both events. Specifically, at 0745:50 UT, the data reveals that V_y = −8.6 km/s, while at 0747:12 UT, the bulk speed along y axis is given by V_y = 22 km/s. This implies that the Doppler shift in these two instances is negligible and does not affect the above wave analysis.

4. Summary and Discussions

[26] We perform continuous wavelet analysis to investigate in detail the electric and magnetic perturbations of the excited waves during current disruption detected by a THEMIS satellite on 29 January 2008. On the basis of the

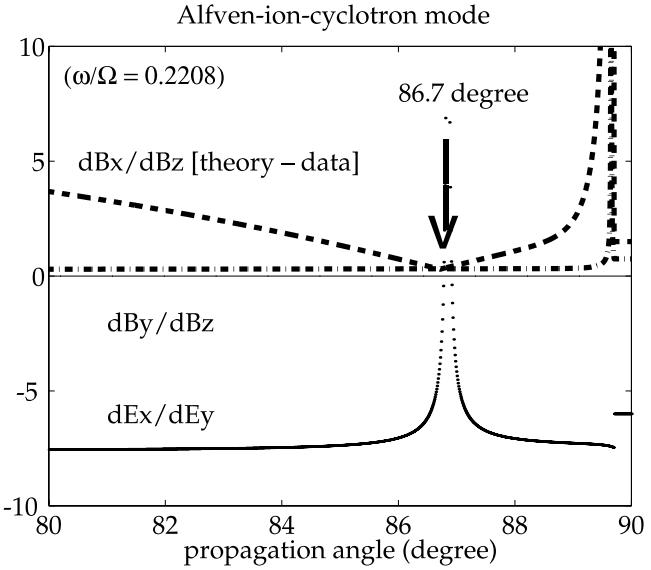

Figure 9c. The same Figure 9a, but for ω/Ω_i = 0.2208.

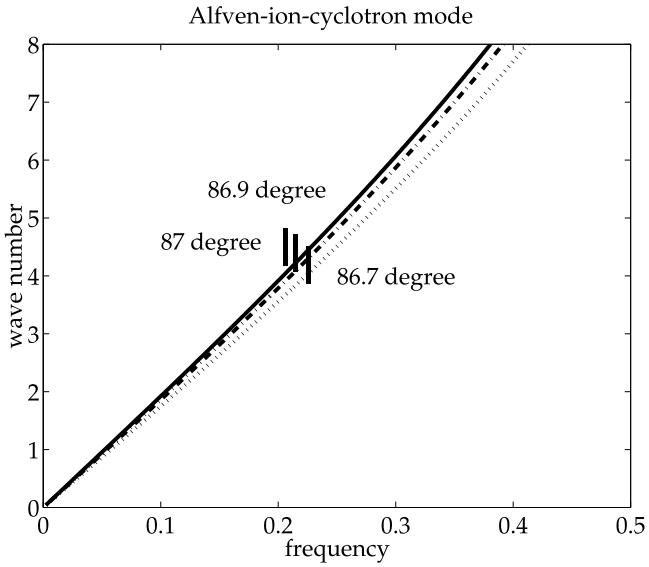

Figure 10. Alfvén ion cyclotron dispersion relation (k versus ω) for three angles: $\theta = 87°$ (top curve), 86.9° (middle curve), and 86.7° (bottom curve).

perturbations extracted from the wavelet analysis, we formulate a procedure to conduct plasma wave diagnostics to identify the instability responsible for these excited waves. Two modes of instability, namely, the drift-driven electromagnetic ion cyclotron instability and the Alfvén ion cyclotron instability, are tested with the wave diagnostics. It is found that the observed wave characteristics resemble that of the waves generated by the Alfvén ion cyclotron instability with propagation angles nearly perpendicular to the local magnetic field.

[27] The present methodology to identify the unstable fluctuations detected in situ by spacecraft can be a powerful diagnostic tool that can help the theorists and modelers to identify the detailed physics associated with the observations. In the future, the present diagnostics must be extended to include thermal effects by considering the full linear dielectric response tensors calculated from Vlasov kinetic theory.

[28] **Acknowledgments.** We thank H. U. Auster and K.-H. Glassmeier for the availability of the FGM data. This work was supported by the NSF grant ATM-0630912 and NASA grant NNX07AU74G to The Johns Hopkins University Applied Physics Laboratory.

[29] Zuyin Pu thanks the reviewers for their assistance in evaluating this paper.

References

Angelopoulos, V. (2008), The THEMIS mission, *Space Sci. Rev.*, *141*, 5–34, doi:10.1007/s11214-008-9336-1.

Auster, U., et al. (2008), The THEMIS fluxgate magnetometer, *Space Sci. Rev.*, *141*, 235–264, doi:10.1007/s11214-008-9365-9.

Bhattacharjee, A., Z. W. Ma, and X. Wang (1998), Dynamics of thin current sheets and their disruption by ballooning instabilities: A mechanism for magnetospheric substorms, *Phys. Plasmas*, *5*, 2001–2009.

Bonnell, J. W., et al. (2008), The Electric Field Instrument (EFI) for THEMIS, *Space Sci. Rev.*, *141*, 303–341, doi:10.1007/s11214-008-9469-2.

Cheng, C. Z., and A. T. Y. Lui (1998), Kinetic ballooning instability for substorm onset and current disruption observed by AMPTE/CCE, *Geophys. Res. Lett.*, *25*, 4091–4094.

Dobias, P., I. O. Voronkov, and J. C. Samson (2004), On linear plasma instabilities during the substorm expansive phase onset, *Phys. Plasmas*, *11*, 2046–2053.

Erickson, G. M., N. C. Maynard, W. J. Burke, G. R. Wilson, and M. A. Heinemann (2000), Electromagnetics of substorm onsets in the near-geosynchronous plasma sheet, *J. Geophys. Res.*, *105*(A11), 25,265–25,290.

Haerendel, G. (1992), Disruption, ballooning or auroral avalanche, in *Proceedings of the First International Conference on Substorms*, *Eur. Space Agency Spec. Publ., ESA SP-335*, 417–420.

Kan, J. R. (2007), On the formation of near-Earth X-line at substorm expansion onset, *J. Geophys. Res.*, *112*, A01207, doi:10.1029/2006JA012011.

Le Contel, Ø., A. Roux, S. Perraut, R. Pellat, O. Holter, A. Pedersen, and A. Korth (2001), Possible control of plasma transport in the near-Earth plasma sheet via current-driven Alfvén waves ($f \approx f_{H+}$), *J. Geophys. Res.*, *106*, 10,817–10,827.

Lee, L. C., L. Zhang, A. Otto, G. Choe, and H. Cai (1998), Entropy antidiffusion instability and formation of a thin current sheet during geomagnetic substorms, *J. Geophys. Res.*, *103*, 29,419–29,428.

Liu, W. W. (1997), Physics of the explosive growth phase: Ballooning instability revisited, *J. Geophys. Res.*, *102*, 4927–4931.

Lui, A. T. Y., and A.-H. Najmi (1997), Time-frequency decomposition of signals in a current disruption event, *Geophys. Res. Lett.*, *24*, 3157–3160.

Lui, A. T. Y., et al. (1991), A cross-field current instability for substorm expansions, *J. Geophys. Res.*, *96*, 11,389–11,401.

Lui, A. T. Y., P. H. Yoon, C. Mok, and C.-M. Ryu (2008a), Inverse cascade feature in current disruption, *J. Geophys. Res.*, *113*, A00C06, doi:10.1029/2008JA013521.

Lui, A. T. Y., et al. (2008b), Determination of the substorm initiation region from a major conjunction interval of THEMIS satellites, *J. Geophys. Res.*, *113*, A00C04, doi:10.1029/2008JA013424.

Lyons, L. R., S. Liu, J. M. Ruohoniemi, S. I. Solovyev, and J. C. Samson (2003), Observations of dayside convection reduction leading to substorm onset, *J. Geophys. Res.*, *108*(A3), 1119, doi:10.1029/2002JA009670.

Mende, S. B., et al. (2008), The THEMIS array of ground-based observatories for the study of auoral substorms, *Space Sci. Rev.*, *141*, 357–387, doi:10.1007/s11214-008-9380-x.

Perraut, S, et al. (2000), Current-driven electromagnetic ion cyclotron instability at substorm onset, *J. Geophys. Res.*, *105*, 21,097–21,107.

Pu, Z. Y., et al. (1999), Ballooning instability in the presence of a plasma flow: A synthesis of tail reconnection and current disruption models for the initiation of substorms, *J. Geophys. Res.*, *104*, 10,235–10,248.

Roux, A., S. Perraut, P. Robert, A. Morane, A. Pedersen, A. Korth, G. Kremser, B. Aparicio, D. Rodgers, and R. Pellinen (1991), Plasma sheet instability related to the westward traveling surge, *J. Geophys. Res.*, *96*, 17,697–17,714.

Sarafopoulos, D. V. (2008), A physical mechanism producing suprathermal populations and initiating substorms in the Earth's magnetotail, *Ann. Geophys.*, *26*, 1617–1639.

Shiokawa, K., W. Baumjohann, and G. Haerendel (1997), Braking of high-speed flows in the near-Earth tail, *Geophys. Res. Lett.*, *24*, 1179–1182.

Swift, D. W., and Y. Lin (2001), Substorm onset viewed by a two-dimensional, global-scale hybrid code, *J. Atmos. Sol. Terr. Phys.*, *63*, 683–704.

Voronkov, I., R. Rankin, P. Frycz, V. T. Tikhonchuk, and J. C. Samson (1997), Coupling of shear flow and pressure gradient instabilities, *J. Geophys. Res.*, *102*(A5), 9639–9650.

J. W. Bonnell, Space Sciences Laboratory, University of California, Berkeley, CA 94720, USA.

A. T. Y. Lui, Johns Hopkins University Applied Physics Laboratory, Laurel, MD 20723-6099, USA.

P. H. Yoon, IPST, University of Maryland, College Park, MD 20742, USA. (yoonp@umd.edu)